Nanoscale

PAPER

View Article Online
View Journal

Cite this: DOI: 10.1039/d6nr00094k

Neutrophil-lifecycle-inspired nanoplatform for the treatment of lung cancer bone metastasis

Yan Xu,†[a,b] Minyu Li,†[c,d] Boheng Liu,[a,b] Shilin Li,[e] Qian Zheng,[a,b] Yanlu Xiong,[a,b,f] Ru Bai,[g] Yang Liu*[a,b] and Yongfu Ma *[b]

Received 8th January 2026,
Accepted 13th April 2026

DOI: 10.1039/d6nr00094k

rsc.li/nanoscale

Difficulty in achieving effective drug concentration in bone metastasis has been a major challenge for tumor treatment because of the complex physiological environment of bone. Existing bone-targeting nanoparticles exhibit insufficient active targeting capability which relies on the binding of bisphosphonates and calcium. Hence, based on the homing property of aged neutrophils, we construct a C–X–C motif chemokine receptor 4 (CXCR4) targeting peptide, E5 peptide, modified liposome delivery system (D_E5-LPs) loaded with doxorubicin (DOX) that enables specific anchorage of nanoparticles to CXCR4^{hi} aged neutrophils and enhances drug accumulation in bone metastasis. The D_E5-LPs effectively inhibit tumor growth and reduce systemic toxicity induced by chemotherapeutic drugs in a murine model of lung adenocarcinoma bone metastasis. Collectively, this study presents an effective strategy for bone-targeting drug delivery and expands therapeutic strategies for bone-related diseases.

1. Introduction

Lung cancer is one of the most frequently diagnosed cancers and a leading cause of cancer-related mortality worldwide with an estimated 2 million new lung cancer cases and 1.76 million lung cancer-related deaths per year.[1] Lung cancer bone metastasis has attracted increasing attention, as distant metastasis is the primary cause of lung cancer-related deaths and approximately 30–40% of lung cancer patients develop bone metastasis.[2,3] It is strongly associated with poorer prognosis, increased risks of bone pain, spinal cord compression, and pathological fractures compared to other metastatic sites. About 53.4% of patients with bone metastases experience skeletal-related events (SREs) and their median survival is limited to 10 months without active treatment.[4] Besides unfavorable clinical outcomes, low blood perfusion of bone marrow, namely blood–bone marrow barrier,[5] significantly limits drug delivery, posing a key therapeutic challenge for lung cancer bone metastasis.

To solve the dilemma, a large number of nanocarriers of different sizes[6] and with special modifications such as functional molecules,[7] peptides[8] or antibodies[9] have been developed to realize bone targeting drug delivery. Among various targeting functional molecules, the bisphosphonates (BPs) were widely used due to their strong ability to chelate with calcium ions of osseous hydroxyapatite.[10,11] However, the BP-functionalized nanoparticles couldn't specifically target bone lesion because of non-specific accumulation in random bone area. Meanwhile, BP-modified nanoparticles encounter challenges in crossing endothelial and targeting the bone marrow with low blood perfusion, due to the passive targeting effects of BPs.

Therefore, it's crucial to develop an active bone-targeting strategy for treatment. The recently developed cell-based delivery strategy seems to offer a promising and feasible solution.[12,13] It has been observed that C–X–C motif chemokine receptor 4 (CXCR4) expression of neutrophils is progressively upregulated over the lifecycle.[14] Concurrently, aged neutrophils with high CXCR4 spontaneously migrate to bone marrow with high concentration of C–X–C motif chemokine ligand 12 (CXCL12) driven by CXCR4/CXCL12 signal pathway and undergo apoptosis ultimately. Based on these findings, neutrophil hitchhiking strategy was developed in which aged neutrophils transport nanoparticles to bone marrow.[15] Similarly, osteoprogenitor cells have been used to deliver drugs and have achieved significant therapeutic efficiency.[12,16]

[a]Postgraduate School, Medical School of Chinese PLA, Beijing 100853, China
[b]Department of Thoracic Surgery, the First Medical Center of Chinese PLA General Hospital, Beijing 100853, China. E-mail: liuyang301x@sina.com, yongfuabc@sina.com
[c]Academician Workstation, Affiliated Hospital of North Sichuan Medical College, Nanchong 637000, China
[d]Department of Cardiology, Affiliated Hospital of North Sichuan Medical College, Nanchong 637000, China
[e]University of Chinese Academy of Sciences, Beijing 100049, China
[f]Department of Thoracic Surgery, Tangdu Hospital, Fourth Military Medical University, Xi'an, China
[g]CAS Key Laboratory for Biomedical Effects of Nanomaterials and Nanosafety and CAS Center for Excellence in Nanoscience, New Cornerstone Science Laboratory, National Center for Nanoscience and Technology of China, Beijing 100190, China
†These authors contributed equally to this work.

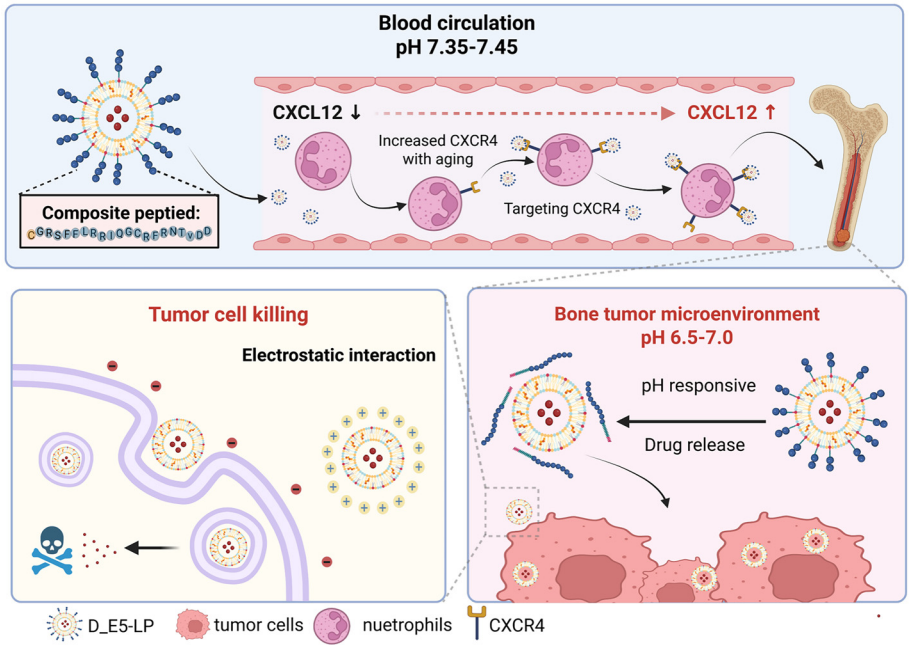

Fig. 1 Schematic diagram of neutrophil hitchhiking liposomes for treatment of lung cancer bone metastasis. D_E5-LPs specifically bind to the surface of aged neutrophils and deliver drugs to the tumor site *via* neutrophil homing. Subsequently, liposomes responsively disassemble in acid TME, enhancing drug uptake of tumor cells. The figure was created with Biorender (https://www.biorender.com).

However, controlling the life cycle of neutrophils *in vitro* remains challenging, as neutrophils have a short lifespan with a half-life of about 19 hours,[14] and only aged neutrophils migrate to the bone marrow. Furthermore, as terminally differentiated cells, neutrophils possess a limited lifespan and lack proliferative capacity, rendering them incapable of sustained expansion or passaging *in vitro*. Consequently, for therapeutic applications, they must be derived directly from patient sources.[14,17,18]

Hence, the strategy that enables nanomaterials to bind to aged ($CXCR4^{hi}$) neutrophils *in vivo*, rather than through *in vitro* co-culture, is more conducive to clinical translation. Modifying nanoparticles with peptides is a promising approach for targeting delivery.[19,20] Studies demonstrated that peptide-modified nanoparticles could bind to activated neutrophils in circulation and deliver drugs.[21] Consequently, we hypothesized that nanoparticles could bind to aged neutrophils by targeting CXCR4. For active targeting, we selected the E5 peptide, an engineered peptide that targets CXCR4, as a guiding molecule to recognize aged neutrophils, exhibiting a concentration-dependent affinity for CXCR4.[22] Although the E5 peptide is widely used in nanomedicine delivery for active targeting of nanoparticles,[23–25] its application for neutrophils targeting has not been reported yet.

Guided by this concept, the E5 peptide may serve as the basis for active targeting aged neutrophils by nanoparticles. 1,2-Distearoyl-*sn-glycero*-3-phosphoethanolamine-hydrazone-polyethylene glycol-E5 (DSPE-HYD-PEG_{2000}-E5) was first synthesized *via* Michael addition reaction to serve as lipid component of liposomes (E5-LPs) preparation through a typical thin-film hydration method.[26] Upon intravenous injection, E5-LPs are expected to spontaneously bind aged neutrophils *in vivo*. Preferential bone-lesion targeting was demonstrated in a murine model of lung cancer bone metastasis established *via* intratibial injection. By loading antitumor chemotherapeutic drug DOX, the system achieved significant therapeutic efficacy (Fig. 1). This study developed a drug delivery system capable of spontaneously binding aged neutrophils in circulation for treatment of tumor bone metastases, revealing a universal bone lesion-targeting platform for various bone diseases.

2. Materials and methods

2.1. Materials

1,2-Distearoyl-*sn-glycero*-3-phosphoethanolamine-hydrazone-(polyethylene glycol)-maleimide (DSPE-HYD-PEG_{2000}-MAL) and 1,2-diacyl-*sn-glycero*-3-phosphocholine (soybean) (HSPC) were purchased from Ruixi Biological Technology Co., Ltd (Xi'an, China). DOX, cholesterol and DOTAP were purchased from Aladdin Biochemical Technology Co., Ltd (Shanghai, China). E5 peptide was obtained from GL Biochem Co., Ltd (Shanghai, China). DiO and Calcein-AM/PI, Live/Dead Cell Double Stain Kit was purchased from Solarbio Science & Technology Co., Ltd (Beijing, China), DiR was obtained from ShareBio Co., Ltd (Shanghai, China), D-luciferin potassium salt was purchased from YangGuangBio Life Sciences Co.,

Ltd (Beijing, China), Cell Membrane Red Fluorescent Staining Kit (Dil) was purchased from Beyotime Co., Ltd (Beijing, China).

2.2 Cell and animals

Lewis lung carcinoma (LLC) cells and LLC cells stably expressing high level of Luciferase (LLC-LUC) were obtained from Fenghui Biotechnology Co., Ltd (Hunan, China) and maintained in Dulbecco's Modified Eagle Medium (DMEM) (Wisent, Canada) supplemented with 10% fetal bovine serum (FBS) (VivaCell, New Zealand) and 1% penicillin streptomycin (Wisent, Canada). Primary neutrophils were isolated and cultured in RPMI 1640 (Wisent, Canada) culture medium containing 10% inactivated FBS and 1% streptomycin–penicillin, as published previously.[15] All cells were maintained at 37 °C and 5% CO_2 in a humidified atmosphere.

Female C57BL/6 mice (6–8 weeks) and SD rats were purchased from the specific pathogen-free (SPF) Biotechnology Co., Ltd (Beijing, China) and housed under conditions of a light/dark cycle of 12 h, an ambient temperature of 25 ± 2 °C, and a humidity of 60 ± 10%. All the animals were treated according to the Guide for Care and Use of Laboratory Animals, and all relevant animal experiments were performed in compliance with the protocols approved by the institutional Animal Care and Use Committee (animal license: NCNST21-202508-0077 and NCNST21-202507-0069) of the National Center for Nanoscience and Technology, Chinese Academy of Sciences.

2.3. Single-cell analysis

The single-cell transcriptomic datasets of 3 lung cancer bone metastasis cases, 12 normal bone tissues, and peripheral blood from lung cancer patients were sourced from the BioProject database (accession code PRJNA1129208[27]) and the Gene Expression Omnibus (GEO) database (accession codes GSE253355 [28] and GSE250001 [29]). R language software (version 4.4.2, https://www.r-project.org) was used to analyze and visualize the single-cell data. Quality control of raw data were performed using the Seurat package (version 5.3.1). Anchor-based integration analysis was performed for lung cancer bone metastasis data to eliminate heterogeneity between samples, while sample integration analysis was conducted by the Harmony package (version 1.2.4) for the peripheral blood data. Finally, neutrophil populations were annotated based on canonical marker genes reported in the original literature and visualized for validation.

2.4. Clinical correlation analysis and survival prognosis analysis

The expression patterns and prognostic significance of CXCR4 in lung cancer were evaluated by analyzing The Cancer Genome Atlas (TCGA) and GEO datasets. Based on the TCGA cohort, the CXCR4 expression levels in lung adenocarcinoma (LUAD) and lung squamous cell carcinoma (LUSC) and their correlation with clinical staging were assessed. Subsequently, Kaplan–Meier survival analysis was performed on patient groups defined by the optimal cutoff of CXCR4 expression. Furthermore, the association between CXCR4 expression and overall survival (OS) in non-small cell lung cancer (NSCLC; GSE14814,[30] GSE50081 [31]), LUAD (TCGA, GSE68465 [32]), and LUSC (TCGA, GSE4573 [33]) cohorts were evaluated. Additionally, the one-year post-surgery disease-free survival (DFS) in the GSE8894 [34] cohort was analyzed with the landmark analysis conducted to mitigate early-event bias. Finally, multivariate Cox regression analysis confirmed CXCR4 expression level as an independent predictor of overall survival.

2.5. Preparation and characterization of DSPE-HYD-PEG-E5

DSPE-HYD-PEG_{2000}-E5 was synthesized as reported previously.[35] Briefly, E5 and DSPE-HYD-PEG_{2000}-MAL with a molar ratio of 1.5 : 1 were dissolved in PBS, containing 1 mM EDTA. Then, the solution was stirred at room temperature under nitrogen protection for 12 h. The excess E5 was removed *via* dialysis against deionized water (MWCO = 3500 Da) for 48 h, followed by lyophilization. The Fourier transform infrared spectroscopy (FTIR) spectra was measured with Micro FT Infrared Spectroscopy (Spotlight 200i, PerkinElmer instruments Co., Ltd, USA).

2.6. Synthesis of E5-LP nanoparticles

E5-LPs was prepared by the film dispersion method. Briefly, HSPC (15 mg), cholesterol (7.5 mg), and DOTAP (5 mg) were dissolved in ethanol and evaporated to form a dried lipid film (40 °C, 20 min). Then, the dried lipid film was hydrated with PBS containing DOX (0.85 mg) and DSPE-HYD-PEG_{2000}-E5 (5 mg). Blank-LPs, DOX-loaded liposomes (D_LPs), DiO/DiR-labeled LPs (DiO/DiR_LPs) were prepared as described above. The solution was homogenized for 5 min with an ultrasound probe (SCIENTZ-IID, Xinzhi Biological Company, China). The hydrodynamic size, polydispersity index and zeta potential of D_E5-LPs were determined by dynamic light scattering (DLS, Zeta sizer Nano ZS, Malvern, UK). The size and morphology were analyzed by transmission electron microscopy (TEM, HT7700, Hitachi, Japan). The encapsulation efficiency (EE%) and drug loading (DL%) were measured by UV-vis spectra (Lambda 950, PerkinElmer instruments Co., Ltd, USA) and calculated by the following equations:

$$\mathrm{DL}\% = W_{\text{loaded drug}}/W_{\text{liposome}} \times 100\%$$

$$\mathrm{EE}\% = W_{\text{loaded drug}}/W_{\text{total drug}} \times 100\%$$

where $W_{\text{loaded drug}}$ and W_{liposome} represent the weight of drug in the liposome and weight of all added to the liposome. $W_{\text{total drug}}$ is the weight of drug added to the liposome.

2.7 Drug release of D_E5-LPs *in vitro*

The release profile of DOX from D_E5-LPs was determined using the dialysis-bag method. D_E5-LPs were added into a pre-treated dialysis bag (MWCO 3.5 kDa), the air was gently expelled, and the bag was sealed. The dialysis bag was then immersed in 9 mL of PBS (pH 7.4 or pH 6.5) and shaken at 300 rpm at 37 °C. At 1, 2, 4, 8, 16, 24, 48 and 72 h, 300 μL ali-

quots were withdrawn and immediately replaced with the same volume of fresh pre-warmed medium. The samples were analyzed by UV-vis spectra.

2.8 Analysis of binding mode between neutrophils and E5-LPs

Primary murine immune cells were isolated following the manufacturer's instructions and cultured *in vitro* for 6 h to induce senescence, as published previously.[15,36] The cells (1×10^6 mL^{-1}) were resuspended in complete 1640 medium, plated in 39 mm glass-bottom dishes and allowed to adhere for 30 minutes. Then complete medium containing DiO_E5-LPs was added and further incubated for 2 h. Cells were maintained alive and were not fixed or permeabilized. On completion of the incubation time, cell components were stained with Dil and Hoechst 33342 and fixed with 4% paraformaldehyde in the dark at room temperature, visualizing, and photographing through Confocal Laser Scanning Microscope (SLM980 Airyscan2, Carl Zeiss, Germany).

2.9 Analysis of binding abilities of LPs to immune cells

DiO served as a fluorescent marker to analyze the binding abilities of liposomes to neutrophils. Murine primary immune cells were isolated and neutrophils were cultured *in vitro* according to the procedures described above.

For neutrophils, the cells (1×10^6 per well) were seeded in 12-well plates and incubated for 6 h. Then, complete medium containing DiO-labeled liposomes (DiO_LPs, DiO_E5-LPs and preincubated DiO_E5-LPs) was added. After incubation of specific duration, the cells were harvested and stained with PE anti-mouse Ly-6G/Ly-6C (Gr-1) antibody and PE/Cyanine5 anti-mouse CD11b antibody (BioLegend, USA) in cell staining buffer, followed by washing and cells were analyzed by CytoFLEX. Data were expressed as mean fluorescence intensities (MFI).

For the different immune cell populations, we referred to the methods described in previous study.[36] Primary mouse bone marrow immune cells were isolated with 6 h culture *in vitro* and seeded into 6-well plates (1×10^6 per well). The cells were cultured in complete medium containing DiO_E5-LPs. After incubation for specific duration, the cells were harvested and stained with 7-AAD Viability Staining Solution, APC/Cyanine7 anti-mouse CD45 Antibody, PE/Cyanine7 anti-mouse/human CD45R/B220 Antibody, and APC anti-mouse CD3 Antibody (BioLegend, USA). Finally, the samples were analyzed by CytoFLEX.

2.10 Hemolysis study

Hemolysis studies with different liposomes were carried out on rat blood sample. Briefly, blood was collected into EDTA containing tubes from adult rats and centrifuged at 2000 rpm for 10 min. Then, the obtained pellet was washed thrice with sterile PBS. Different liposomes were incubated with 5% (v/v) rat erythrocytes at 37 °C for 1 h. The total lipid concentration was the same dose for mice in section 2.14. Consequently, the samples were centrifuged at 2000 rpm for 10 min and the released hemoglobin absorbance at 540 nm was measured. Erythrocytes hemolysis of 100% and 0% after treatment with Triton X-100 and PBS were taken as controls, respectively.

2.11 Biodistribution

8 weeks C57BL/6 mice were inoculated intratibially with LLC-Luc cells (1×10^4 in 10 μl). Five days later, the mice were randomly assigned to two groups, DiR_LPs or DiR_E5-LPs were injected intravenously to the mice. Fluorescence was observed by *In Vivo* imaging System (IVIS) at 1, 2, 4, 8, 12 and 24 h. Afterward, mice were sacrificed and the biodistribution was analyzed by immunofluorescence staining.

2.12 Cellular uptake of nanoparticles

To evaluate the cellular uptake of different liposomes, flow cytometry and inverted fluorescence microscopy were applied.

For flow cytometry, LLC cells (1×10^5 per well) were seeded in 12-well plates and incubated overnight. Then, the cells were incubated with DiO-labeled liposomes as described above. Subsequently, the cells were analyzed *via* flow cytometry at an exciting wavelength (Ex = 484 nm). Data were expressed as MFI.

For inverted fluorescence microscopy, A549 cells were seeded in 12-well plates at a density of 4×10^5 per well and incubated overnight. Subsequently, complete medium containing DOX, D_LPs, D_E5-LPs and preincubated D_E5-LPs of same DOX content were added to the wells and further incubated for 12 h. Then, cells were washed three times with PBS and stained with 1 μg mL^{-1} Hoechst 33342 for 5 minutes. Subsequently, cells were washed and observed through inverted fluorescence microscope (EVOS M5000 Imaging System, Invitrogen, USA).

2.13 *In vitro* cytotoxicity

Cytotoxicity in LLC and A549 cells was investigated by calcein-AM/PI dual staining assay and Cell Counting Kit-8 (CCK-8) assay.

For CCK-8 assay, 1×10^4 LLC cells and 2.5×10^3 A549 cells per well were seeded in 96-well plates and incubated overnight. Subsequently, complete medium containing DOX, D_LP, D_E5-LP and preincubated D_E5-LP of same DOX content were added to the wells and further incubated for 24 h. Then, the cells were washed three times with PBS and medium was replaced with complete medium with 10% CCK-8. After 30 min of incubation, the cell viability was measured with a microplate reader at 450 nm.

For calcein-AM/PI dual staining assay, 2×10^5 LLC and 1×10^5 A549 cells per well were seeded in 12-well plates and incubated with drug or liposomes as described above for 24 h. Afterwards, cell staining was completed with Calcein-AM/PI live/dead cell double staining kit and the cell morphology and fluorescence were captured with an inverted fluorescence microscope.

2.14 *In vivo* antitumor activity

LLC tumor-bearing female C57BL/6 mice were used to evaluate antitumor activity. LLC-Luc cells (1×10^5) were injected into proximal tibias of mice. After 5 days, the mice were randomly assigned to four groups ($n = 5$ biologically independent animal per group): (1) Saline (2) DOX (3) D_LP (4) D_E5-LP. A different formulation of liposomes was injected intravenously at a dosage of 5 mg kg^{-1} DOX every three days for 6 injections. The body weight of the mice was recorded every two days. At the end of the experiment, the mice were euthanized and histopathological analysis (H&E) was conducted on the major organ sections. Blood samples were collected for hematology analyses.

2.15 Micro-CT

The tibias of mice were observed under micro-CT. Images and major bone parameters were analyzed with Imalytics Preclinical software.

2.16 Statistical analysis

All data were presented as the mean ± SD. The statistically significant differences were analyzed by the two-tailed Student's *t*-test (two groups) and a one-way analysis of variance (ANOVA) (multiple groups). The *P* value was calculated with the help of Graphpad Prism. Error bars are expressed as mean ± SD. $*P < 0.05$, $**P < 0.01$, $***P < 0.001$ were considered statistically significant.

3. Results and discussion

3.1. The level of CXCR4 was related to the prognosis of patients with lung cancer and elevated in neutrophils of patients with lung cancer metastasis

CXCR4, the specific receptor for the chemokine CXCL12, is broadly expressed on the surface of diverse tumor cells, and participates in key biological processes including tumor cell invasion, migration and regulation of the tumor microenvironment (TME).[37] To identify the potential role of *CXCR4* in lung cancer progression, we performed an analysis of LUAD samples based on TCGA database. Our results revealed that *CXCR4* expression was negatively correlated with tumor stage in LUAD, which is significantly higher in pathological stage I than in stages III and IV. Within the tumor-node-metastasis (TNM) staging system, *CXCR4* expression at T1 was also markedly higher than at T2 and T4 (Fig. 2a). However, no significant differences in *CXCR4* expression were observed between different age or sexes, and there was no statistically significant association with lymph node metastasis (N stage) or distant metastasis (M stage) (Fig. S1a). Further survival analyses demonstrated that LUAD patients with high *CXCR4* expression had better OS than those with low expression ($P = 0.036$, hazard ratio 0.68, 95% confidence interval 0.47 to 0.97; Fig. 2b). This finding was further validated using an independent external cohort from the GEO database (Fig. 2c). To minimize confounding effects, we conducted multivariate Cox proportional hazards regression analysis; after adjusting for key clinicopathological variables including age, sex, TNM stage and pathological stage, *CXCR4* remained an independent prognostic factor for LUAD ($P = 0.02$; Fig. 2d). Collectively, these results establish *CXCR4* as a robust prognostic biomarker in LUAD.

Unlike its prognostic role in LUAD, the prognostic value of *CXCR4* in LUSC exhibited histology subtype-specific patterns. *CXCR4* expression levels were significantly higher in female patients than in males. However, no significant differences were observed across pathological stage, TNM stage, or ages (Fig. S1b and c). Regarding prognosis, survival analysis of the TCGA cohort did not reveal a significant association between *CXCR4* expression and OS in LUSC (Fig. S1d). In contrast, in an independent external GEO validation cohort, LUSC patients with high *CXCR4* expression exhibited significantly better OS than those with low expression ($P = 0.03$, hazard ratio 0.48, 95% confidence interval 0.26 to 0.93; Fig. 2e).

Despite the heterogeneity within LUSC subtypes, when *CXCR4* was evaluated in a GEO cohort comprising both LUAD and LUSC patients (*i.e.*, non-small cell lung cancer, NSCLC), high *CXCR4* expression was likewise associated with significantly better OS compared with low expression (Fig. S1e and f). Further analysis in another independent cohort investigating its association with postoperative recurrence showed that although *CXCR4* expression was not significantly associated with the overall recurrence rate, the high-expression group had significantly longer DFS (Fig. S1g). Despite inter-subtype histological differences, *CXCR4* retains important prognostic implications in the overall NSCLC population. In summary, the above results indicate that CXCR4 plays a critical role in lung cancer disease trajectory, and low *CXCR4* expression is associated with poor prognosis. However, its application for targeting metastatic tumor cells remains challenging.

Given their dynamic surface CXCR4 and homing capacity, neutrophils have attracted our attention. As the most abundant leukocyte subset in humans, neutrophils exhibit biological behaviors that are precisely regulated by the CXCR4/CXCL12 signaling axis. CXCR4 expression on neutrophils increases progressively during maturation and aging, and aged neutrophils with high CXCR4 levels home to the bone marrow along a CXCL12 chemotactic gradient. These findings provide a biological foundation for leveraging CXCR4 targeting to achieve BM drug delivery. To further investigate the feasibility of neutrophil "hitchhiking" strategy, we performed an integrated analysis of single-cell RNA-sequencing (scRNA-seq) datasets from 12 normal bone tissue samples and 3 NSCLC bone-metastasis samples. Based on neutrophil markers identified within the datasets reported previously (Fig. S1h), we annotated neutrophil populations after dimensionality reduction using uniform manifold approximation and projection (UMAP) (Fig. 2f). We found that the proportion of neutrophils in the bone-metastasis microenvironment was significantly higher compared with that in normal bone tissue.

Furthermore, we analyzed a scRNA-seq dataset of neutrophils derived from peripheral blood of 6 NSCLC patients and

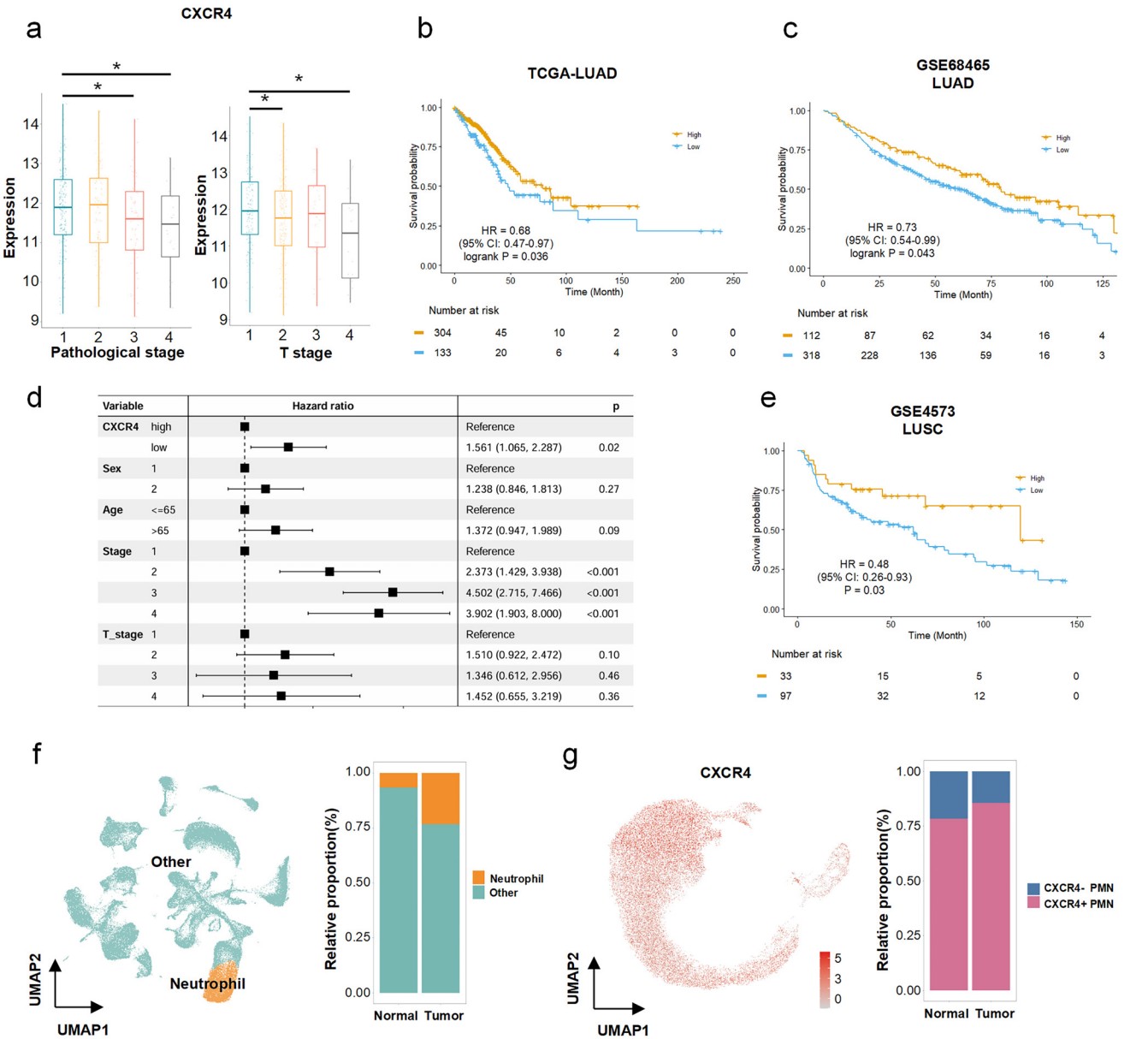

Fig. 2 The correlation between CXCR4 expression and prognosis of patients with lung cancer and evaluated CXCR4 expression level of neutrophil in patients with lung cancer metastasis. (a) Expression level of CXCR4 of different pathological stages and T stages in LUAD. Statistical significance was calculated by one-way ANOVA analysis of variance. *P < 0.05, **P < 0.01. ***P < 0.001. Overall analysis of CXCR4-high-expressing and -low-expressing LUAD from TCGA database (b) and GEO database (c). (d) Multivariate Cox regression analysis of CXCR4 expression and key clinicopathological variables in the TCGA lung adenocarcinoma cohort. (e) Overall analysis of CXCR4-high-expressing and -low-expressing LUSC. (f) (1) The analysis integrates single-cell RNA sequencing data from 12 normal bone and 3 LUAD bone metastasis specimens. The datasets were integrated to establish joint embedding and annotation. (2) The proportion of neutrophil in all cell clusters. (g) (1) UMAP visualization of integrated scRNA-seq profiles of NSCLC and healthy-donor neutrophil populations. (2) The proportion of CXCR4-positive neutrophils across all cell clusters.

7 healthy controls. UMAP visualization following dimensionality reduction revealed that *CXCR4* was broadly expressed among neutrophils. Notably, comparative analysis showed that the proportion of *CXCR4*-positive neutrophils in the peripheral blood of lung cancer patients was higher than that in the control group (Fig. 2g). Collectively, neutrophil "hitchhiking" is a promising strategy for the targeted delivery of drugs to lung cancer bone metastasis.

3.2. Preparation and characterization of E5-LPs

To achieve the neutrophil "hitchhiking" strategy, the surface modification and mechanisms of targeting delivery are illustrated in Fig. 1. E5 peptide was conjugated to 1,2-distearoyl-*sn*-*glycero*-3-phosphoethanolamine-hydrazone-poly (ethylene glycol)-2000-maleimide (DSPE-HYD-PEG$_{2000}$-MAL) *via* Michael addition to endow liposomes with binding capability to aged

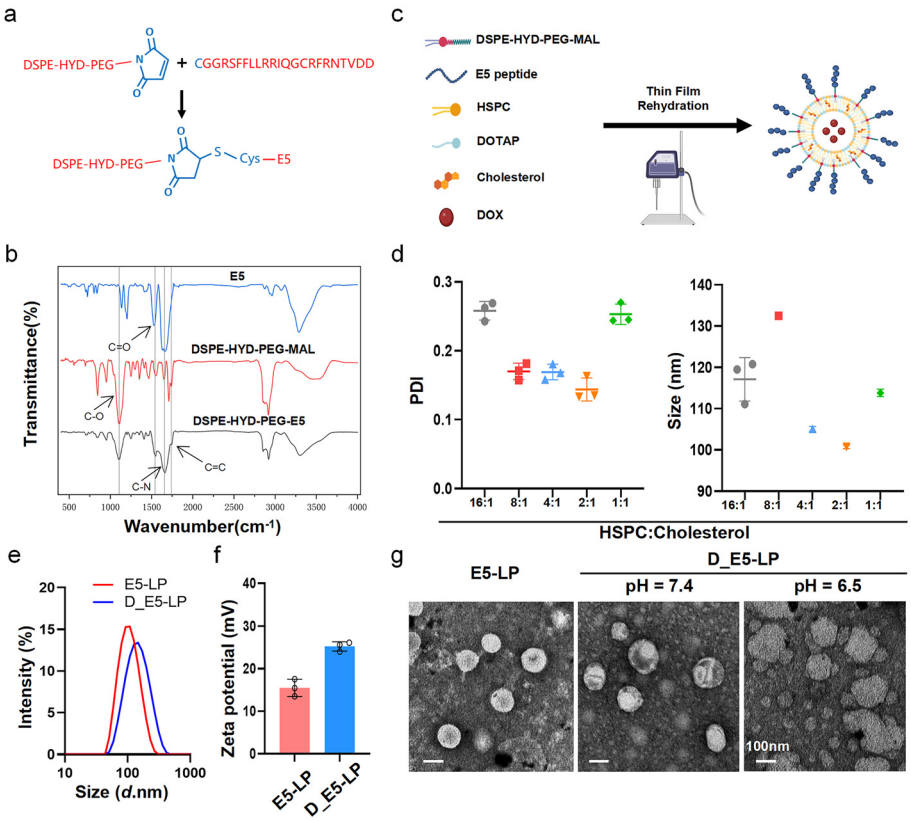

Fig. 3 Synthesis and characterization of liposomes. (a) Schematic illustration for the formation process of DSPE-HYD-PEG-E5. (b) FTIR spectra of DSPE-HYD-PEG-E5, DSPE-HYD-PEG-Mal, and E5 peptide. (c) Synthesis process of E5-LPs. (d)The optimal mass ratio of HSCP : Cholesterol in formulation under the conditions of DSPE-HYD-PEG_{2000}-E5 (5.0 mg), DOTAP (5.0 mg) (n = 3). (e) Hydrodynamic sizes of E5-LPs and D_E5-LPs. (f) Zeta potential of E5-LPs and D_E5-LPs. (g) TEM images of E5-LPs, D_E5-LPs and D_E5-LPs after incubation at pH 6.5 buffer. Scale bar = 100 nm.

($CXCR4^{hi}$) neutrophils, (Fig. 3a). Successful synthesis of DSPE-HYD-PEG_{2000}-E5 was characterized by FTIR spectrum. FTIR spectrum of DSPE-HYD-PEG_{2000}-E5 as displayed in (Fig. 3b), a PEG characteristic peak (C–O) at 1106 cm^{-1} was clearly observed, while the C=C stretching vibration peak at 1739 cm^{-1} was attenuated. Regarding the spectra of E5 peptide, the peaks at around 1542 cm^{-1} and 1658 cm^{-1} indicated amide I (carbonyl C=O and guanidine C–N stretching peak) and amide II (C–N stretching peak and N–H bending peak), respectively. DSPE-HYD-PEG_{2000}-E5 was also confirmed using ^{1}H-Nuclear Magnetic Resonance (NMR), with the characteristic peaks of E5 peptide at 7.25 ppm and from 1.14 ppm to 3.19 ppm, characteristic peaks of PEG at 3.61 ppm and diminished characteristic peak of MAL at 7.0 ppm (Fig. S2). These results demonstrated the successful synthesis of DSPE-HYD-PEG_{2000}-E5.

E5 peptide modified liposomes (D_E5-LPs) were constructed using a thin film hydration technique (Fig. 3c). To obtain an optimal E5-LPs, we screened a series of liposomes with different mass ratio of cholesterol (Fig. 3d). The results showed that D_E5-LPs with HSPC : cholesterol = 2 : 1 (mass ratio) exhibited the smallest particle size and the narrowest size distribution. The hydrodynamic diameters of E5-LPs and D_E5-LPs were 100 nm and 132 nm (Fig. 3e), respectively, with zeta potentials of +17 mV and +21 mV (Fig. 3f). Consistently, the transmission electron microscopy (TEM) results showed that, D_E5-LPs were larger than E5-LPs (Fig. 3g), confirming successful loading of DOX. For D_E5-LPs, the encapsulation efficiency (EE) and drug loading efficiency (DL) of DOX were 90.9% and 2.3% (mass fraction), respectively.

To verify the acid-responsive properties of D_E5-LPs, we characterized its DOX release and morphology in weakly acidic conditions. The cumulative release of D_E5-LPs was 32% (pH 7.4) and 53% (pH 6.5) after 24 h incubation, indicating the release of DOX was acid-dependent and time-dependent (Fig. S3b). Notably, TEM image displayed the irregularity of D_E5-LPs in pH 6.5 buffer (Fig. 3g). We imply that the acidic-sensitive release behavior was caused by responsive partial hydrolysis of hydrazone bond and disassembly of PEG.

Collectively, we successfully constructed E5 peptide-functionalized liposomes with effective drug-loading capacity and acid-responsiveness.

3.3. Targeting ability of E5-LPs *in vitro* and *in vivo*

To determine whether E5-LPs binds to neutrophils, DiO-labeled liposomes were synthesized and were incubated with murine aged neutrophils. Immunofluorescence imaging revealed that DiO_E5-LPs localized on neutrophil membrane

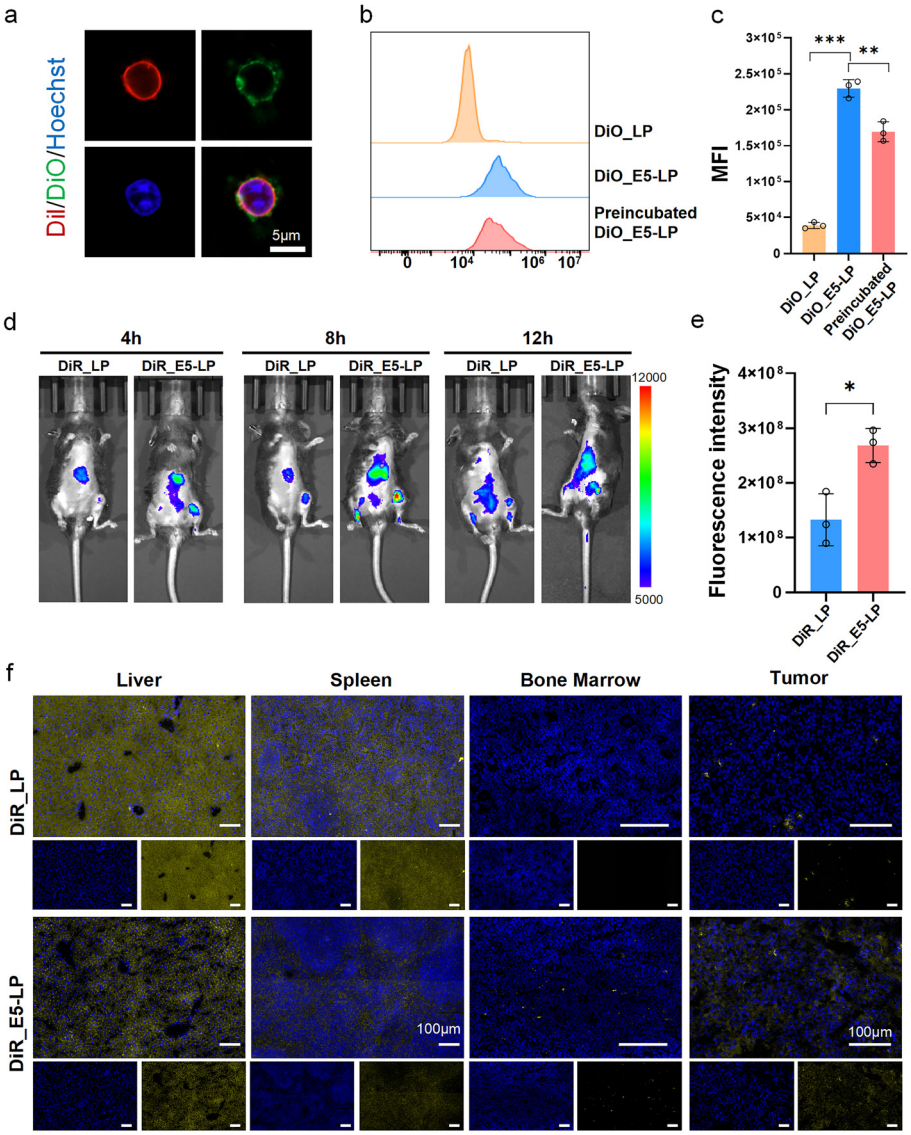

Fig. 4 Targeting ability of D_E5-LPs *in vivo* and *in vitro*. (a) CLSM images of murine aged neutrophils incubated with DiO_E5-LPs (green). Cells were stained with Hoechst 33342 (blue) and DiI (red). Scale bar = 5 μm. (b) Flow cytometric analysis of binding between murine aged neutrophils and NPs (n = 3 biologically independent experiments). (c) Quantitative analysis of DiO fluorescence was determined (n = 3 biologically independent experiments). Data are presented as mean ± SD. Statistical significance was calculated by one-way ANOVA analysis of variance. *P < 0.05, **P < 0.01, ***P < 0.001. (d) IVIS imaging tumor bearing mice after intravenous injection of DiR_LPs or DiR_E5-LPs. (e) Histograms of DiR signal of both groups after 8 h of intravenous injection. Statistical significance was determined by unpaired two-tailed t-test. *P < 0.05. (f) Fluorescence images of liver, spleen, bone marrow and tumor 12 h after intravenously injection of DiR_LPs or DiR_E5-LPs. scale bars = 100 μm.

surface without being internalized into cytoplasm (Fig. 4a). To further assess how E5 modification affects LP binding to neutrophils, murine neutrophils were incubated with DiO_LPs, DiO_E5-LPs, or acid-treated DiO_E5-LPs, and then cellular fluorescence was quantified. Flow cytometric analysis demonstrated that E5 modification markedly enhanced the binding capacity of LPs to neutrophils compared with unmodified LPs. Meanwhile, binding ability of DiO_E5-LPs to aged neutrophils was markedly reduced after preincubation at pH 6.5, in which the E5 peptide was detached, confirming that E5-LPs had pH-sensitive properties (Fig. 4b and c). In addition, the fluorescence intensity of each group increased as the incubation time increased, showing a time-dependent change (Fig. S4). To further investigate the potential off-target effects of E5-LPs, we examined their binding capacity to distinct immune cell populations. Previous studies have shown that CXCR4 is widely expressed on the surface of various immune cells, including neutrophils, monocytes, and T lymphocytes.[38,39] Accordingly, we assessed the binding of DiO_E5-LPs to primary mouse immune cells by flow cytometry and fluorescence microscopy. The results showed that nanoparticle-positive cells were primarily neutrophils (Fig. S5c). 61.38% ± 1.21% of neutrophils

were positive for nanoparticles, whereas the percentages in monocytes (26.03% ± 5.20%) and T cells (29.33% ± 2.81%) were significantly lower (Fig. S5d). These results verified that E5-LPs presented enhanced and specific *in vitro* neutrophil-binding capability and pH-sensitive dissociation property.

The improved neutrophil-binding capability of E5-LPs was designed to increase the accumulation of nanocarriers at bone metastatic sites compared with unmodified LPs. Therefore, we aimed to validate the *in vivo* biodistribution of the material in tumor-bearing mice. Prior to these studies, the biosafety of LPs was first assessed. The hemolysis test was performed and results showed good biocompatibility with 2–4% hemolysis of LPs and E5-LPs, 5–9% hemolysis of D_LPs and D_E5-LPs for their high positive surface charge (Fig. S6). To evaluate *in vivo* targeting capability of E5-LPs, a murine lung cancer bone metastasis model was established *via* intratibial injection. The DiR was encapsulated in nanoplatform to track its biodistribution *in vivo*. Tumor-bearing mice with confirmed tumor formation at day 12 post-inoculation were intravenously administered DiR-labeled liposomes. Across all examined time points, after 4, 8, and 12 hours of intravenous injection, DiR_E5-LPs consistently exhibited superior accumulation in bone tumor regions compared with DiR_LPs (Fig. 4d). Notably, at 8 h post-administration, the fluorescence signal in tumors peaked, and DiR_E5-LPs exhibited 2.03-fold higher fluorescence in bone lesions than DiR_LPs (Fig. 4e), indicating efficient targeting. Furthermore, the targeting specificity of DiR_E5-LPs was verified by immunofluorescence staining. DiR_E5-LP group exhibited higher fluorescence intensity in tumor tissue and bone marrow of tumor-bearing side, but lower intensity in liver and spleen compared to DiR_LP group (Fig. 4f and Fig. S7). Collectively, these results demonstrated that E5-LPs exhibited specific targeting to bone metastasis in mice with reduced off-target distribution in other organs.

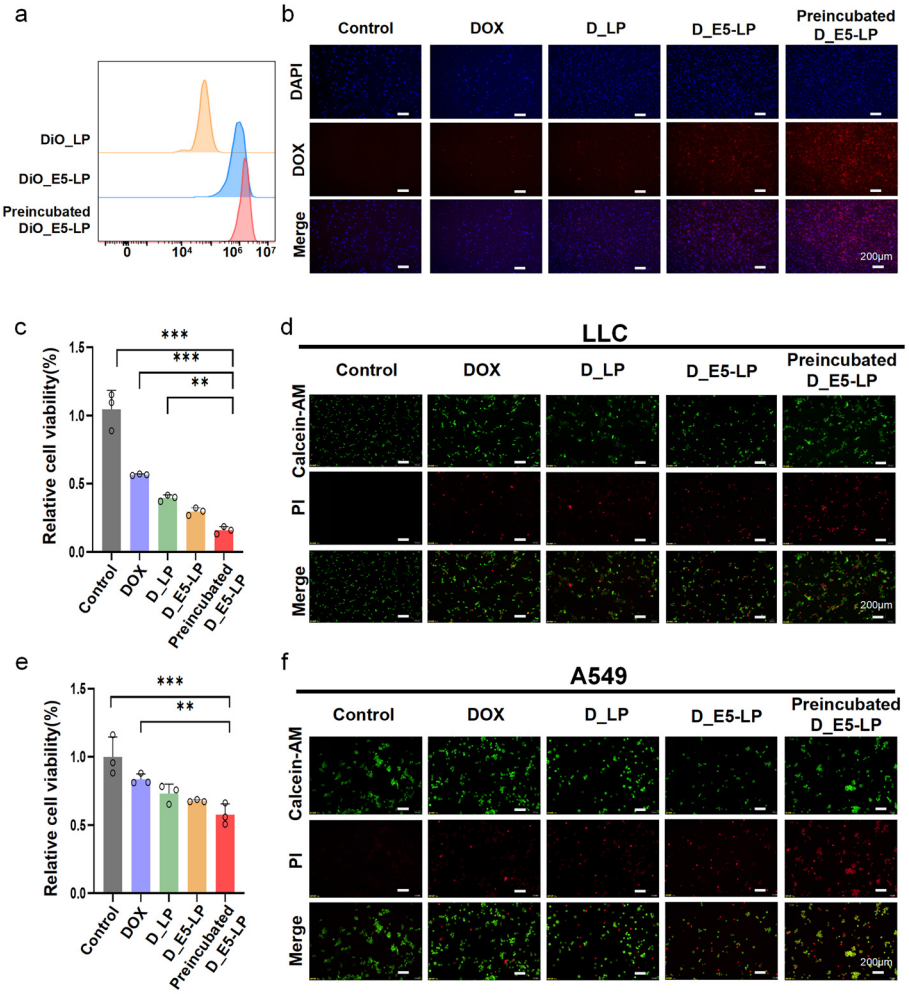

Fig. 5 Cellular uptake and tumoricidal ability of D_E5-LPs. (a) The representative histograms of flow cytometric analysis of LLC uptake. (b) Fluorescence microscopy images of A549 uptake (n = 3 biologically independent experiments). Cell viability of LLC (c) /A549 (e) and fluorescence staining results of live (green) or dead (red) for LLC (d) /A549 (f) with different treatment of liposomes. Scale bar = 200 μm. Data are presented as mean ± SD. Statistical significance was calculated by one-way ANOVA analysis of variance. *P < < 0.05, **P < 0.01, ***P < 0.001. Preincubated D_E5-LPs: D_E5-LPs were preincubated with PBS (pH = 6.5).

3.4. Improved *in vitro* antitumor activity

In our study, targeting-neutrophils E5 peptide was conjugated to the surface of E5-LPs *via* pH-sensitive hydrazone bonds, enabling rapid dissociation from neutrophils in TME and higher cellular uptake efficiency. Flow cytometry was used to evaluate *in vitro* uptake of liposomes by tumor cells. As expected, cellular accumulation of DiO_E5-LPs and acid-treated DiO_E5-LPs was significantly increased compared with unmodified DiO_LPs (Fig. 5a). Besides, tumor cells exhibited higher uptake of acid-treated DiO_E5-LPs than untreated DiO_E5-LPs. Notably, the cellular uptake of DiO_E5-LPs was enhanced by targeting peptide conjugated to the receptor on the surface, since CXCR4 is expressed on various tumor cells, including lung cancer.[40,41] Furthermore, DiO_E5-LP group showed higher drug uptake under acidic conditions. Such enhancement stems from hydrazone bond hydrolysis and PEG detachment under acidic environments, which weakened the steric barrier imposed by dense PEG coating and promoted cellular uptake.[42,43] Additionally, cellular uptake efficiency was assessed by analyzing DOX signal following incubation using inverted fluorescence microscope. As shown, A549 cells treated with free DOX displayed weak red fluorescent signals after incubation, whereas incubation with D_LPs induced stronger intracellular red fluorescence intensity. Consistent with the results of flow cytometry, the brightest intracellular red fluorescence was observed following acid-preincubated D_E5-LP group (Fig. 5b), further confirming the effectiveness of the acid-responsive system.

Increased intracellular accumulation of DOX contributes to inhibition of tumor cell proliferation and promotion of tumor cell apoptosis. LLC and A549 cell lines, as typical lung cancer cell lines, were widely used in cytotoxicity assessment, mechanistic studies, and evaluation of antitumor activity.[44,45] Therefore, they were selected for experiments to evaluate antitumor activity. The experimental results obtained by CCK-8 assay demonstrated that DOX, D_LPs, D_E5-LPs, and acid-preincubated D_E5-LPs effectively inhibited tumor cell viability within 24 hours, in which acid-preincubated D_E5-LP group showed the strongest inhibition, followed by D_E5-LP group and D_LP group, while free DOX group was the weakest (Fig. 5c and e). Consistent results were obtained using Calcein-AM/PI double staining assays (Fig. 5d and f). As expected, compared with other groups, the red fluorescence signal of acid-preincubated D_E5-LP group was enhanced, while the green fluorescence signal was weakened. Almost half of the cells

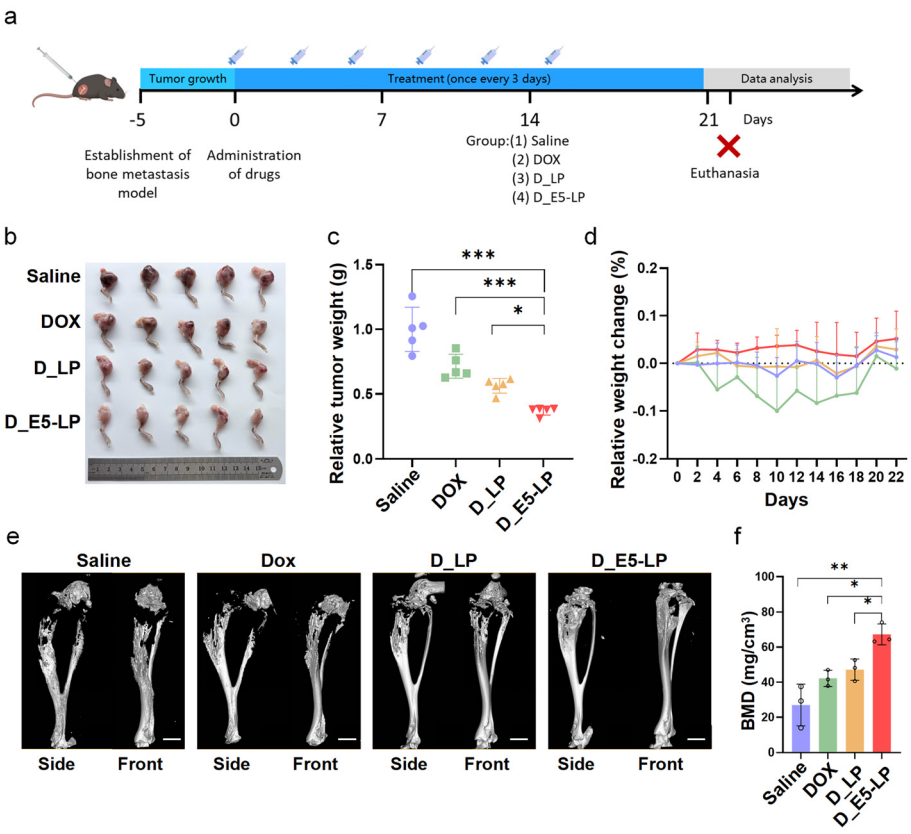

Fig. 6 Antitumor efficiency of D_E5-LPs *in vivo*. (a) Schematic description of LLC-Luc bone metastasis tumor model in C57BL/6 mice. (b) Morphology of mice legs at the site of metastasis in all groups at 22 days. (c) Relative tumor weight of excised tumor tissue in all groups (n = 5). (d) Relative weight changes of mice during treatment. (e) Representative micro-CT images of the femurs and tibias in each group. Scale bar = 2 mm. (f) Relative BMD of the tibias calculated by the software 3D Slicer (n = 3). The data were presented as mean ± SD. Statistical significance was calculated by one-way ANOVA analysis of variance. *P < 0.05, **P < 0.01, ***P < 0.001.

were in a dead state (red), suggesting that acid-preincubated D_E5-LPs had a potent antitumor effect.

In summary, D_E5-LPs, particularly acid-treated D_E5-LPs, exhibited excellent *in vitro* antitumor activity, which may be attributable to the increased intracellular accumulation of drugs.

3.5. Anti-tumor effect of reduced-toxicity E5-LPs against bone metastasis

Encouraged by the antitumor and targeting capacity of D_E5-LPs, we further assessed its therapeutic efficacy *in vivo*. Accordingly, we established a lung cancer bone metastasis model by intratibial injection. The experiment design is depicted in Fig. 6a. After 3 weeks of treatment, mice in D_E5-LP group had the smallest tumor size and weight (Fig. 6b and c). Furthermore, the micro-CT images showed that the tibias had serious osteolytic lesions in all groups except D_E5-LP group (Fig. 6e). The osteolytic lesions were related to calcium loss during tumor progression, and D_E5-LPs prevented bone mineral density (BMD) loss (Fig. 6f), demonstrating the best inhibitory effect on lung cancer bone metastasis.

To evaluate the safety of liposomes *in vivo*, the white blood cell count (WBC), red blood cell count (RBC), platelet count (PLT), and hemoglobin (Hb) of the mice were tested to assess myelosuppression at the end of the pharmacodynamic experiment. These results demonstrated that the free DOX could significantly reduce the number of WBC and PLT, and the D_E5-LPs showed reduced drug-induced toxicity (Fig. 7a). Besides, mice of DOX group exhibited a significant reduction in body weight after treatment, whereas D_E5-LP group showed no statistically significant difference (Fig. 6d), demonstrating D_E5-LPs could effectively mitigate drug-induced toxicity. Furthermore, to assess potential organ toxicity, hematoxylin and eosin (H&E) staining of main organs, including the heart, liver, spleen, lung and kidney, was performed. No histological alteration was observed in normal cells within these organs, indicating an absence of toxicity in these tissues (Fig. 7b). Notably, no significant differences were observed in the organ

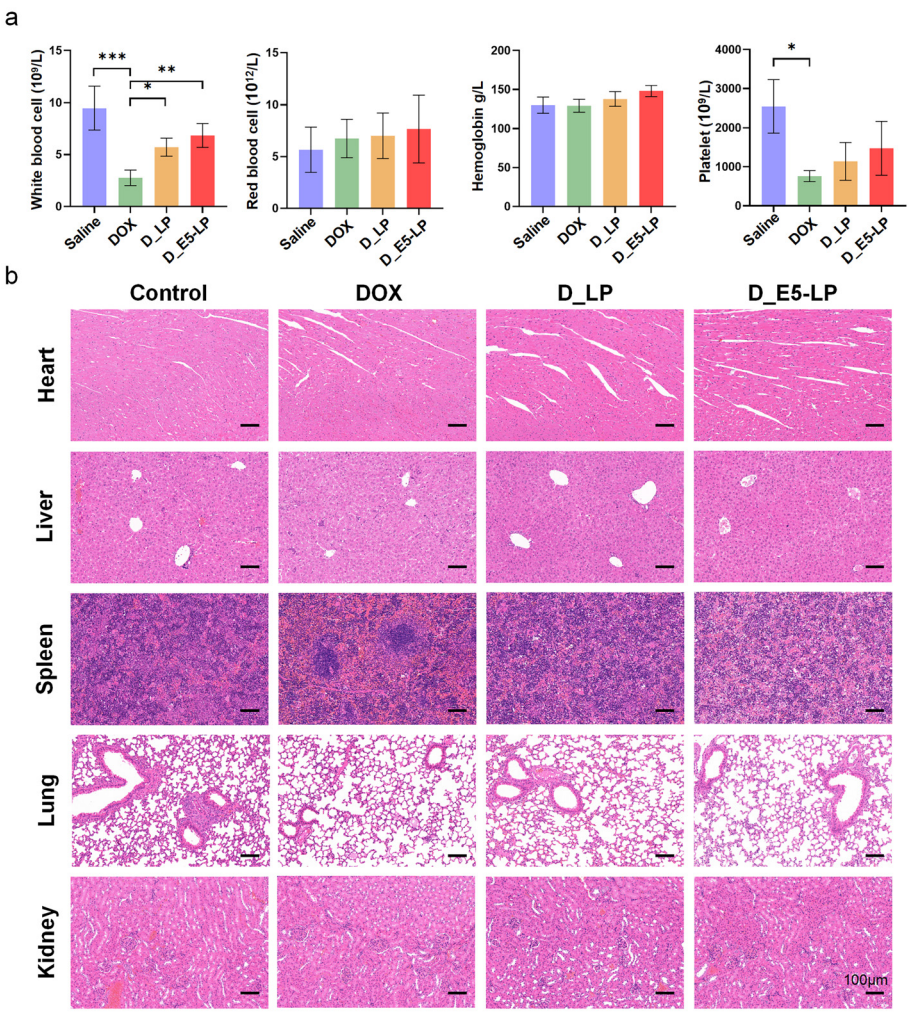

Fig. 7 Safety evaluation of D_E5-LPs *in vivo*. (a) The hematologic parameters (WBC, RBC, Hb and PLT) in the whole blood were determined. The data were presented as mean ± SD. Statistical significance was calculated by one-way ANOVA analysis of variance. (b) Representative histological images (200×) of the H&E stained heart, liver, spleen, lung and kidney, harvested from the mice. Scale bar = 100μm.

coefficients among groups, with the exception of the spleen (Fig. S8a). Tumor-bearing mice in the saline, DOX and D_LP groups suffered more from splenomegaly than mice in the D_E5-LP group (Fig. S8b and c).

Collectively, these findings suggest that D_E5-LP is effective against lung cancer bone metastasis while reducing the off-target toxicity associated with DOX.

4. Conclusion

In summary, our study developed acid-responsive liposomes (E5-LPs) based on neutrophil "hitchhiking" strategy for treating lung cancer bone metastasis. E5-LPs exhibited excellent neutrophil-binding capacity both *in vitro* and *in vivo*, enabling delivery of chemotherapeutic drug to bone marrow and reduced off-target distribution, thereby lessening the side effects. Furthermore, E5-LPs disassemble in response to acid TME, enhancing cellular uptake by tumor cells and increasing therapeutic efficacy. Collectively, our work provides a platform that delivers drugs to bone metastases and enhances tumor-site accumulation, offering promising clinical application prospects.

Author contributions

Conceptualization: Yan Xu, Yongfu Ma; investigation: Yan Xu, Minyu Li, Boheng Liu, Shilin Li; visualization: Yan Xu, Minyu Li, Boheng Liu, Shilin Li, Qian Zheng, Yanlu Xiong, Ru Bai; writing – original draft preparation: Yan Xu, Minyu Li; review and editing: Yongfu Ma, Yang Liu; supervision: Yongfu Ma; funding acquisition: Yongfu Ma, Ru Bai. All authors have read and agreed to the published version of the manuscript.

Conflicts of interest

The authors declare that they have no known competing financial interests or personal relationships that could have appeared to influence the work reported in this paper.

Data availability

All data needed to support the conclusions are present in the paper or the supplementary information (SI). Supplementary information is available. See DOI: https://doi.org/10.1039/d6nr00094k.

Additional data related to this paper are available from the corresponding author upon reasonable request.

Acknowledgements

Financial support for this research was provided by the Beijing Natural Science Foundation (Grant No. 7262015), Health Care Special Research Project of Military Logistics Research Program (Grant No. 23BJZ23), National Major Scientific Instrument Development Project (Grant No. 32527801).

References

1 F. Bray, M. Laversanne, H. Sung, J. Ferlay, R. L. Siegel, I. Soerjomataram and A. Jemal, *CA Cancer J. Clin.*, 2024, **74**, 229–263.
2 Z. Liu, M. Zhang, S. Han, H. Zhang, S. Meng, Z. Shen and X. Ma, *Cancer Rep.*, 2025, **8**, e70211.
3 W. Chen, R. Zheng, P. D. Baade, S. Zhang, H. Zeng, F. Bray, A. Jemal, X. Q. Yu and J. He, *CA Cancer J. Clin.*, 2016, **66**, 115–132.
4 S. Hong, T. Youk, S. J. Lee, K. M. Kim and C. M. Vajdic, *PLoS One*, 2020, **15**, e0234927.
5 M. Tavassoli, *Br. J. Haematol.*, 1979, **41**, 297–302.
6 I. M. Adjei, B. Sharma, C. Peetla and V. Labhasetwar, *J. Controlled Release*, 2016, **232**, 83–92.
7 H. Zhang, S. Wu, W. Chen, Y. Hu, Z. Geng and J. Su, *Bioact. Mater.*, 2023, **23**, 156–169.
8 S. Wang, B. Li, H. Zhang, J. Chen, X. Sun, J. Xu, T. Ren, Y. Zhang, C. Ma, W. Guo and K. Liu, *Angew. Chem., Int. Ed.*, 2021, **60**, 11252–11256.
9 Z. Tian, L. Wu, C. Yu, Y. Chen, Z. Xu, I. Bado, A. Loredo, L. Wang, H. Wang, K. L. Wu, W. Zhang, X. H. Zhang and H. Xiao, *Sci. Adv.*, 2021, **7**, eabf2051.
10 S. Jiang, S. Li, S. Liao, J. Jiang, K. Xu, X. Tian, Q. Zheng, J. Zhang, J. Mei, X. Wang, J. Yuan, Y. Liu and Y. Ma, *Nano Today*, 2024, **57**, 102338.
11 L. Xue, N. Gong, S. J. Shepherd, X. Xiong, X. Liao, X. Han, G. Zhao, C. Song, X. Huang, H. Zhang, M. S. Padilla, J. Qin, Y. Shi, M. G. Alameh, D. J. Pochan, K. Wang, F. Long, D. Weissman and M. J. Mitchell, *J. Am. Chem. Soc.*, 2022, **144**, 9926–9937.
12 Y. Chen, Q. W. Chen, F. S. Fu, H. Y. Gu, A. Yu and X. Z. Zhang, *ACS Nano*, 2024, **18**, 29864–29879.
13 W. Ma, Y. Yang, B. Yang, B. Tang, L. Bai, Y. He, Y. Li and Y. Lin, *Adv. Mater.*, 2025, **37**, e05714.
14 A. Hidalgo, E. R. Chilvers, C. Summers and L. Koenderman, *Trends Immunol.*, 2019, **40**, 584–597.
15 Z. Luo, Y. Lu, Y. Shi, M. Jiang, X. Shan, X. Li, J. Zhang, B. Qin, X. Liu, X. Guo, J. Huang, Y. Liu, S. Wang, Q. Li, L. Luo and J. You, *Nat. Nanotechnol.*, 2023, **18**, 647–656.
16 E. Udofa and Z. Zhao, *Adv. Drug Delivery Rev.*, 2024, **204**, 115143.
17 T. M. Fliedner, E. P. Cronkite, S. A. Killmann and V. P. Bond, *Blood*, 1964, **24**, 683–700.
18 J. T. Dancey, K. A. Deubelbeiss, L. A. Harker and C. A. Finch, *J. Clin. Invest.*, 1976, **58**, 705–715.
19 K. Li, C. J. Liu and X. Z. Zhang, *Adv. Drug Delivery Rev.*, 2020, **160**, 36–51.

20 C. Hu, J. Ma, X. Chen, Y. Chen, Y. Song, Q. Tang, X. He, Y. Wang, H. Gao and J. Zhang, *Sci. Adv.*, 2025, **11**, eadu5245.
21 M. A. Cruz, D. Bohinc, E. A. Andraska, J. Alvikas, S. Raghunathan, N. A. Masters, N. D. van Kleef, K. L. Bane, K. Hart, K. Medrow, M. Sun, H. Liu, S. Haldeman, A. Banerjee, E. M. Lessieur, K. Hageman, A. Gandhi, M. de la Fuente, M. T. Nieman, T. S. Kern, C. Maas, S. de Maat, K. B. Neeves, M. D. Neal, A. Sen Gupta and E. X. Stavrou, *Nat. Nanotechnol.*, 2022, **17**, 1004–1014.
22 X. Li, H. Guo, Y. Yang, J. Meng, J. Liu, C. Wang and H. Xu, *Sci. Rep.*, 2014, **4**, 6610.
23 J. Meng, Y. Ge, H. Xing, H. Wei, S. Xu, J. Liu, D. Yan, T. Wen, M. Wang, X. Fang, L. Ma, Y. Yang, C. Wang, J. Wang and H. Xu, *Small*, 2020, **16**, e2001890.
24 H. Bai, Q. Sun, F. Kong, H. Dong, M. Ma, F. Liu, C. Wang, H. Xu, N. Gu and Y. Zhang, *J. Mater. Chem. B*, 2021, **9**, 5245–5254.
25 M. Wang, R. Guo, Y. Zhao, Y. Wang, W. Fu, G. Wang, M. Lu, H. a. Wu, M. Ma, Y. Bai and Y. Zhang, *Nano Res.*, 2025, **18**, 94908016.
26 X. Wang, X. Wang, J. Su, D. Wang, W. Feng, X. Wang, H. Lu, A. Wang, M. Liu and G. Xia, *ACS Nano*, 2024, **18**, 27917–27932.
27 X. Zhang, K. Xiao, Y. Wen, F. Wu, G. Gao, L. Chen and C. Zhou, *Nat. Commun.*, 2024, **15**, 9855.
28 S. Bandyopadhyay, M. P. Duffy, K. J. Ahn, J. H. Sussman, M. Pang, D. Smith, G. Duncan, I. Zhang, J. Huang, Y. Lin, B. Xiong, T. Imtiaz, C. H. Chen, A. Thadi, C. Chen, J. Xu, M. Reichart, Z. Martinez, C. Diorio, C. Chen, V. Pillai, O. Snaith, D. Oldridge, S. Bhattacharyya, I. Maillard, M. Carroll, C. Nelson, L. Qin and K. Tan, *Cell*, 2024, **187**, 3120–3140.
29 C. Lattanzi, F. Bianchetto-Aguilera, M. Donini, F. Pettinella, E. Caveggion, M. Castellucci, S. Gasperini, B. Mariotti, I. Signoretto, M. Cantini, S. Pilotto, L. Belluomini, C. Tecchio, F. Bazzoni, S. Brandau, N. Tamassia, M. A. Cassatella and P. Scapini, *OncoImmunology*, 2025, **14**, 2521396.
30 C. Q. Zhu, K. Ding, D. Strumpf, B. A. Weir, M. Meyerson, N. Pennell, R. K. Thomas, K. Naoki, C. Ladd-Acosta, N. Liu, M. Pintilie, S. Der, L. Seymour, I. Jurisica, F. A. Shepherd and M. S. Tsao, *J. Clin. Oncol.*, 2010, **28**, 4417–4424.
31 S. D. Der, J. Sykes, M. Pintilie, C. Q. Zhu, D. Strumpf, N. Liu, I. Jurisica, F. A. Shepherd and M. S. Tsao, *J. Thorac. Oncol.*, 2014, **9**, 59–64.
32 K. Shedden, J. M. Taylor, S. A. Enkemann, M. S. Tsao, T. J. Yeatman, W. L. Gerald, S. Eschrich, I. Jurisica, T. J. Giordano, D. E. Misek, A. C. Chang, C. Q. Zhu, D. Strumpf, S. Hanash, F. A. Shepherd, K. Ding, L. Seymour, K. Naoki, N. Pennell, B. Weir, R. Verhaak, C. Ladd-Acosta, T. Golub, M. Gruidl, A. Sharma, J. Szoke, M. Zakowski, V. Rusch, M. Kris, A. Viale, N. Motoi, W. Travis, B. Conley, V. E. Seshan, M. Meyerson, R. Kuick, K. K. Dobbin, T. Lively, J. W. Jacobson and D. G. Beer, *Nat. Med.*, 2008, **14**, 822–827.
33 M. Raponi, Y. Zhang, J. Yu, G. Chen, G. Lee, J. M. Taylor, J. Macdonald, D. Thomas, C. Moskaluk, Y. Wang and D. G. Beer, *Cancer Res.*, 2006, **66**, 7466–7472.
34 E. S. Lee, D. S. Son, S. H. Kim, J. Lee, J. Jo, J. Han, H. Kim, H. J. Lee, H. Y. Choi, Y. Jung, M. Park, Y. S. Lim, K. Kim, Y. Shim, B. C. Kim, K. Lee, N. Huh, C. Ko, K. Park, J. W. Lee, Y. S. Choi and J. Kim, *Clin. Cancer Res.*, 2008, **14**, 7397–7404.
35 S. Fu, L. Chang, S. Liu, T. Gao, X. Sang, Z. Zhang, W. Mu, X. Liu, S. Liang, H. Yang, H. Yang, Q. Ma, Y. Liu and N. Zhang, *Nat. Commun.*, 2023, **14**, 2248.
36 T. G. Dacoba, N. Nabar and P. T. Hammond, *ACS Nano*, 2025, **19**, 11333–11347.
37 F. Balkwill, *Semin. Cancer Biol.*, 2004, **14**, 171–179.
38 A. Rueda, N. Serna, R. Mangues, A. Villaverde and U. Unzueta, *Biomark. Res.*, 2025, **13**, 68.
39 O. Wald, O. M. Shapira and U. Izhar, *Theranostics*, 2013, **3**, 26–33.
40 R. J. Phillips, M. D. Burdick, M. Lutz, J. A. Belperio, M. P. Keane and R. M. Strieter, *Am. J. Respir. Crit. Care Med.*, 2003, **167**, 1676–1686.
41 Y. Yang, J. Li, W. Lei, H. Wang, Y. Ni, Y. Liu, H. Yan, Y. Tian, Z. Wang, Z. Yang, S. Yang, Y. Yang and Q. Wang, *Int. J. Biol. Sci.*, 2023, **19**, 3341–3359.
42 L. J. Cruz, P. J. Tacken, R. Fokkink and C. G. Figdor, *Biomaterials*, 2011, **32**, 6791–6803.
43 W. Gao and L. Zhang, *Nat. Mater.*, 2025, **24**, 1682–1683.
44 J. G. Mayo, W. R. Laster Jr., C. M. Andrews and F. M. Schabel Jr., *Cancer Chemother. Rep., Part 1*, 1972, **56**, 183–195.
45 M. Lieber, B. Smith, A. Szakal, W. Nelson-Rees and G. Todaro, *Int. J. Cancer*, 1976, **17**, 62–70.